ACS OMEGA

Open Access

http://pubs.acs.org/journal/acsodf

Article

Tuning the Electronic and Optical Properties of Crystalline Anthracene by Doping and Pressure for Photovoltaic Applications

Congqing Yang* and Xuan Luo

Cite This: *ACS Omega* 2025, 10, 4143−4153

Read Online

ACCESS | Metrics & More | Article Recommendations

ABSTRACT: Despite their numerous advantages, organic molecular crystals are often unsuitable for photovoltaic applications due to their poor optoelectronic properties. Here we employ density functional theory to show that the combination of substitutional doping and hydrostatic pressure can effectively tune the structural, electronic, and optical properties of crystalline anthracene. Specifically, we aim to reduce the electronic band gap of crystalline anthracene in order to improve its optical absorption, so that the modified materials become suitable for use in solar cells. Our results reveal that lattice parameters and bond lengths decrease with pressure, hence strengthening interactions between atoms and narrowing the band gap. Doping also reduces the band gap significantly. In the end, three materials studied in the current research display close-to-ideal band gaps: O-doped anthracene under 8.75 GPa of pressure (1.353 eV), P-doped anthracene under 10 GPa (1.073 eV), and S-doped anthracene under 2.5 GPa (1.341 eV). Furthermore, they exhibit high absorption coefficient values on the order of 10^5 cm^{-1} within the visible light range, a noteworthy improvement over pure anthracene. Therefore, we have successfully tuned the optoelectronic properties of crystalline anthracene and identified three ideal candidates for solar cell materials.

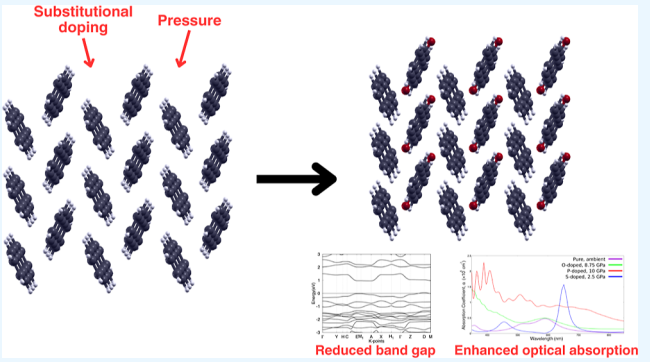

1. INTRODUCTION

Fossil fuels currently account for 82% of the global energy consumption.[1] Its use has created and aggravated numerous global problems, such as climate change and air pollution, all the while posing significant public health risks.[2] As a result, substantial attention has been turned to renewable energy, with particular emphasis on photovoltaics (PV). PV cells, or solar cells, convert the energy of sunlight into electricity by using semiconductors. The evolution and various iterations of this technology can be categorized into three generations. First-generation solar cells are made of thick films of crystalline silicon.[3] As of now, they account for 90% of the PV market and 80% of installed capacity due to their stability, long life span, and relatively high power conversion efficiencies (PCE) which range from 15% to 25%, with 29.4% being the current theoretical record.[3−5] However, these solar cells are also expensive, inflexible, difficult to maneuver, and sensitive to high temperatures.[3] Second-generation solar cells employ thin films, typically on the micrometer scale, of materials including amorphous silicon, cadmium telluride, and gallium indium copper diselenide.[6] Although thin film technology allows for flexibility and reduced costs, their PCEs are drastically reduced to about 10%−15%.[3] Third-generation solar cells encompass a wide variety of innovative technology: dye-sensitized solar cells (DSSCs), quantum dot solar cells (QDSCs), perovskite solar cells (PVSCs), tandem solar cells (TSCs), and organic solar cells (OSCs).[3,7] Among these, OSCs, which implement carbon-based small molecules or polymers as their building blocks, are of particular interest due to their low cost, lightweight, flexibility, nontoxicity, band gap tunability, and high absorption coefficients.[8−11] However, the most pressing problem that OSCs face is their low PCE, meaning they harness considerably less solar energy than other types of solar cells. Hence, significant research has been dedicated to improving this crucial aspect of OSCs.

As the key component in OSCs, organic semiconductors play a crucial role in determining the cells' effectiveness. In particular, single crystal organic semiconductors exhibit great potential for PV applications. This is because research has shown that high crystallinity and long-range order are conducive to high charge carrier mobilities,[12−14] minimal traps and defects,[15] charge transport,[16] exciton diffusion,[17,18] and charge separation[19]—characteristics closely tied with a solar cell's efficiency. In 2013, Sim et al. investigated the

Received: December 1, 2024
Revised: January 13, 2025
Accepted: January 17, 2025
Published: January 24, 2025

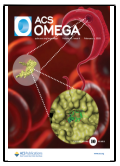

dependence of exciton diffusion length upon crystallinity in P3HT films, and found that exciton diffusion length increased more than 2-fold with increasing crystallinity.[20] The work of Lunt et al. on crystalline perylenetetracarboxylic dianhydride (PTCDA) further confirmed this dependence.[14] Additionally, Verreet et al. showed that crystallized thin amorphous rubrene films demonstrated diffusion lengths of at least 200 nm as well as a fill factor of 66%.[21] These results underscore the great potential of single crystal organic semiconductors in PV applications.

One group of materials that demonstrates promising signs of application in organic photovoltaics is polyacenes, a class of π-conjugated molecules which consist of linearly fused benzene rings. These molecules can vary in the number of rings; for instance, the anthracene molecule has three rings, tetracene has four, and pentacene has five. Polyacenes have been shown to display high thermal stability, high carrier mobility,[22] and high open-circuit voltage,[23] making them good candidates for solar cell materials. Furthermore, since polyacenes are small molecules, they show high reproducibility and small batch-to-batch variations, a crucial advantage over polymers which makes possible their mass production with high accuracy.[23] Considering the aforementioned advantages of crystalline materials, crystalline polyacenes (which are organic molecular crystals) exhibit great potential for application in OSCs. However, polyacenes tend to have large band gaps within the range of 2−4 eV according to theoretical and experimental reports.[24−26] This means that polyacenes, in their pure forms, will be rather ineffective if used in solar cells according to the Shockley−Queisser limit, which states that the ideal band gap for solar cell semiconductors should be within 1.0−1.6 eV if a >30% cell efficiency is desired.[27] Therefore, mechanisms such as doping and the application of pressure to polyacenes have been studied as a means of reducing their band gap. For instance, Fedorov used density functional theory (DFT) to observe changes in the band gaps of crystalline anthracene and tetracene up to 30 GPa of pressure; his work demonstrated that the band gap decreased steadily as pressure increased, reaching 1.62 eV (anthracene) and 0.31 eV (tetracene) at 30 GPa, a promising result.[28] The work of Hummer et al. demonstrated a similar correlation between the band gap and applied pressure for crystalline anthracene. They also observed a redshift in the optical absorption spectra as well as a broadening of absorption peaks, further strengthening the case for using pressure to tune anthracene's electronic and optical properties.[29] Muz et al. substitutionally doped pentacene molecules with 3d transition metals and found the resulting energy gaps to be in the range of 0.33−4.44 eV. Though their work focuses on molecules, it sheds light on the effectiveness of doping at tuning the band gap of polyacenes.[30] Thus, we have taken inspiration from these works and investigated the effects of both substitutional doping and the application of pressure on crystalline anthracene.

In this study, we employed density functional theory to analyze the effects of substitutional doping and application of hydrostatic pressure on crystalline anthracene. Specifically, we studied four systems: pure anthracene, oxygen-doped anthracene, phosphorus-doped anthracene, and sulfur-doped anthracene. Structural, electronic, and optical properties of these four systems were calculated for varying pressures up to 20 GPa. In Section 2, we detailed our methods to perform first-principle calculations. Section 3 presents and discusses our results. Our conclusion is found in Section 4.

2. METHOD

2.1. Computational Details. We performed first-principle calculations based on density functional theory (DFT) using the generalized gradient approximation (GGA) within the Perdew−Burke−Ernzerhof (PBE) format as implemented in the ABINIT code.[31] We used the projected augmented wave (PAW) method[32] to generate pseudopotentials with the ATOMPAW code.[33] The electron configurations and radius cut-offs of the elements used in the current research are listed in Table 1.

Table 1. Electron Configuration and Radius Cutoff of Elements Used in the Current Research

element	electron configuration	radius cutoff (bohr)
hydrogen (H)	$1s^1$	0.995
carbon (C)	$[He]2s^22p^2$	1.507
oxygen (O)	$[He]2s^22p^4$	1.415
phosphorus (P)	$[Ne]3s^23p^3$	1.907
sulfur (S)	$[Ne]3s^23p^4$	1.915

Total energy calculations using self-consistent field (SCF) iterations were considered converged when the difference in total energy between two adjacent iterations was less than 1.0×10^{-10} hartree twice consecutively. The kinetic energy cutoff and Monkhorst−Pack k-point grids were considered converged when the difference in total energy between two adjacent data sets was less than 1.0×10^{-4} hartree twice successively. Kinetic energy cutoffs were calculated and converged for all individual elements first; using these results, the kinetic energy cutoff of a system was then taken to be the maximum of the cutoffs of the elements composing the system.

2.2. Atomic and Crystal Structures. Initial lattice parameters and atomic positions of the unit cell of ambient crystalline anthracene were obtained from the Cambridge Crystallographic Data Centre.[34] Relaxation calculations using the Broyden−Fletcher−Goldfarb−Shanno (BFGS) algorithm[35−38] were carried out in order to optimize atomic structures. Unit cell angles were kept constant. Lattice constants and atomic positions were relaxed until the maximum forces on each atom in all three directions were below 2.0×10^{-4} hartree/bohr (equivalent to 0.01 eV/angstrom). We performed relaxation calculations for each of the four systems under each of their respective hydrostatic pressures. Afterward, electronic and optical properties were computed using the optimized structural parameters.

2.3. Electronic Structure. The electronic structures of the studied materials were analyzed through band structure and projected density of state (PDOS) calculations. All band structure calculations were carried out using the following set of high-symmetry k-points in the irreducible first Brillouin zone: Γ (0, 0, 0), Y (0.5, 0, −0.5), H (0.58285, 0, −0.19061), C (0.5, 0, 0), E (0.5, 0.5, 0), M_1 (0.41715, 0.5, 0.19061), A (0, 0.5, 0.5), X (0, 0, 0.5), H_1 (0.41715, 0, 0.19061), Γ (0, 0, 0), Z (0, 0.5, 0), D (0.5, 0.5, −0.5), and M (0.58285, 0.5, −0.19061). A detailed description of the Brillouin zone and the corresponding k-path is illustrated in Figure 1. PDOS was calculated for all materials with a k-point mesh of $10 \times 10 \times 10$ using the tetrahedron method in order to further understand atomic orbital contributions to electronic structures.

It is widely recognized that DFT calculations employing the GGA-PBE functional underestimate the band gap value. Therefore, in order to accurately predict our experimental

https://doi.org/10.1021/acsomega.4c10572
ACS Omega 2025, 10, 4143−4153

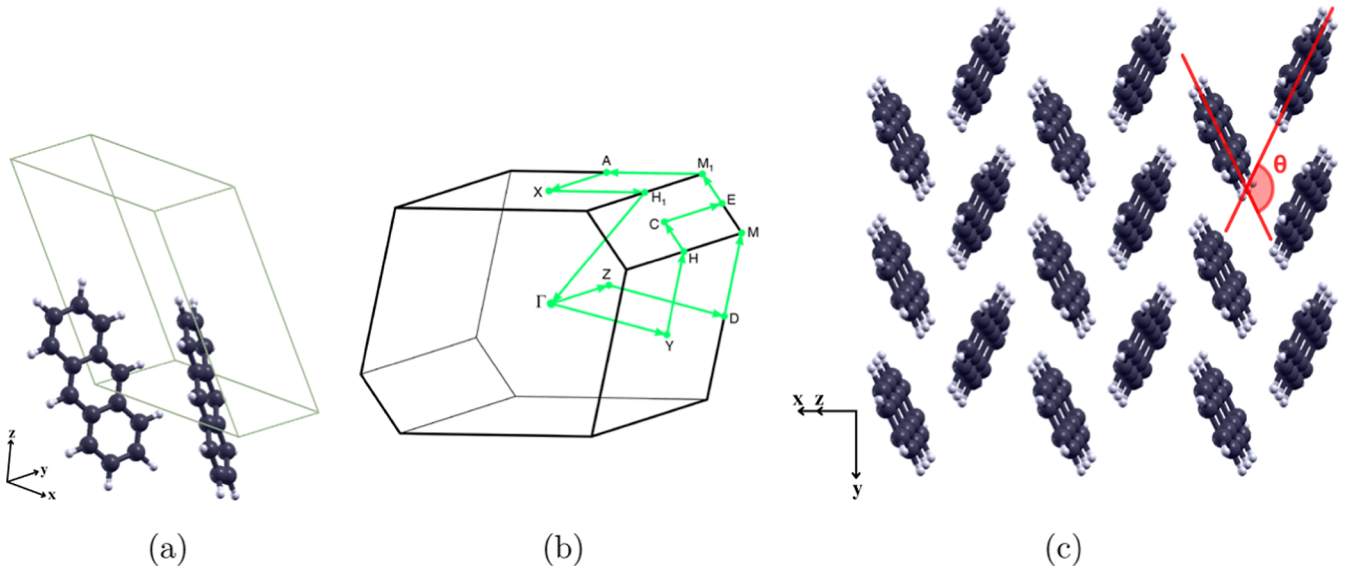

Figure 1. (a) Primitive unit cell of crystalline anthracene. (b) K-path used for band structure calculations. (c) 3 × 3 × 3 supercell demonstrating the crystal structure of anthracene. The concept of the herringbone angle θ is shown as well. Hydrogen atoms are depicted in white, carbon atoms are depicted in gray.

values from our theoretical results, we use the following correction formula[39,40]

$$E_g^c(\text{corrected}) = 0.998 \times (1.358 \times E_g(\text{GGA} - \text{PBE}) + 0.125) + 0.014 \quad (1)$$

where E_g(GGA−PBE) is the band gap value calculated from DFT using General Gradient Approximation within the Perdew−Burke−Ernzerhof format and E_g^c represents the corrected band gap value.

2.4. Optical Properties. The macroscopic dielectric functions of select materials were calculated using the Bethe−Salpeter (BS) approach within the ABINIT package. Standard excitonic calculations within the Tamm-Dancoff approximation (TDA) using the Haydock iterative technique were performed with a 6 × 6 × 6 k-mesh. The Haydock iterations were set to end after the difference between two consecutive evaluations of the macroscopic dielectric function reached less than 0.05 eV. A Γ-centered k-mesh was used to compute the screening of the Coulomb potential while an unsymmetrical k-mesh (shifted along the primitive axis by (0.11, 0.21, 0.31)) was used to construct the transition space for solving the Bethe−Salpeter equation. The value of the scissor operator, which describes how much the conduction bands of a material shift up by, was determined by the difference between the DFT-calculated band gap and corrected band gap (from eq 1) in order to account for DFT-induced underestimation. The energy cutoff for the dielectric matrix, the number of bands, as well as the lowest occupied band used to construct the electron−hole basis in the transition space were subject to convergence studies by checking the convergence of their respective resulting optical absorption spectra.

The macroscopic dielectric function can be expressed in the form[41]

$$\varepsilon(\omega) = \varepsilon_1(\omega) + i\varepsilon_2(\omega) \quad (2)$$

where $\varepsilon_1(\omega)$ and $\varepsilon_2(\omega)$ are the real and imaginary parts of the function, respectively. $\varepsilon_2(\omega)$ describes the optical absorption spectra and is given by[41]

$$\varepsilon_2(\omega) = \frac{2e^2\pi}{\Omega\varepsilon_o} \sum_{k,v,c} |\langle \psi_k^c | \hat{U} \cdot \vec{r} | \psi_k^v \rangle|^2 \delta(E_k^c - E_k^v - E) \quad (3)$$

where E_k^c and E_k^v represent the energy of electrons at a certain k-vector in the conduction and valence bands, respectively, and E is the photon energy. Using the Kramer−Kronig relation, $\varepsilon_1(\omega)$ can be calculated from $\varepsilon_2(\omega)$ using[41]

$$\varepsilon_1(\omega) = 1 + \frac{2}{\pi} P \int_0^\infty \frac{\omega' \varepsilon_2(\omega')}{\omega'^2 - \omega^2} d\omega' \quad (4)$$

From $\varepsilon_1(\omega)$ and $\varepsilon_2(\omega)$, the extinction coefficient $k(\omega)$ and absorption coefficient $(\alpha(\omega))$ can be obtained with[42]

$$k(\omega) = \sqrt{\frac{\sqrt{\varepsilon_1^2(\omega) + \varepsilon_2^2(\omega)} - \varepsilon_1(\omega)}{2}} \quad (5)$$

$$\alpha(\omega) = \frac{4\pi k(\omega)}{\lambda} \quad (6)$$

where λ is the wavelength of light.

3. RESULTS AND DISCUSSION

3.1. Atomic and Crystal Structures. Anthracene ($C_{14}H_{10}$) is a polycyclic hydrocarbon that is composed of three linearly fused benzene rings. It crystallizes in the primitive monoclinic space group $P2_1/c$ and has the lattice parameters a = 16.162 bohr (8.5526 Å), b = 11.368 bohr (6.0158 Å), c = 21.112 (11.1720 Å), $\alpha = \gamma = 90°$, β = 124.596°.[43] As seen in Figure 1a, one unit cell contains two translationally inequivalent anthracene molecules, with one at the corner of the base and another at the center of the base. Anthracene assumes the herringbone packing motif as illustrated in Figure 1c. Figure 1c also illustrates the concept of the herringbone angle θ, which describes how the two anthracene molecules within the unit cell are oriented with

https://doi.org/10.1021/acsomega.4c10572
ACS Omega 2025, 10, 4143−4153

Table 2. Lattice Constants (a, b, c), Unit Cell Volume (V), C−H Bond Length, and Herringbone Angle (θ) of Crystalline Anthracene under Various Applied Hydrostatic Pressures (Lattice Angles Were Kept Constant)

pressure (GPa)	a (bohr)	b (bohr)	c (bohr)	V (bohr^3)	C−H (bohr)	θ (deg)
ambient	16.162	11.368	21.112	3193.095	2.0637	129.563
5	15.233	10.715	19.899	2673.722	2.0592	130.175
10	14.695	10.336	19.196	2400.189	2.0550	130.922
15	14.364	10.103	18.763	2241.337	2.0514	131.310
20	14.117	9.930	18.441	2127.872	2.0476	131.727

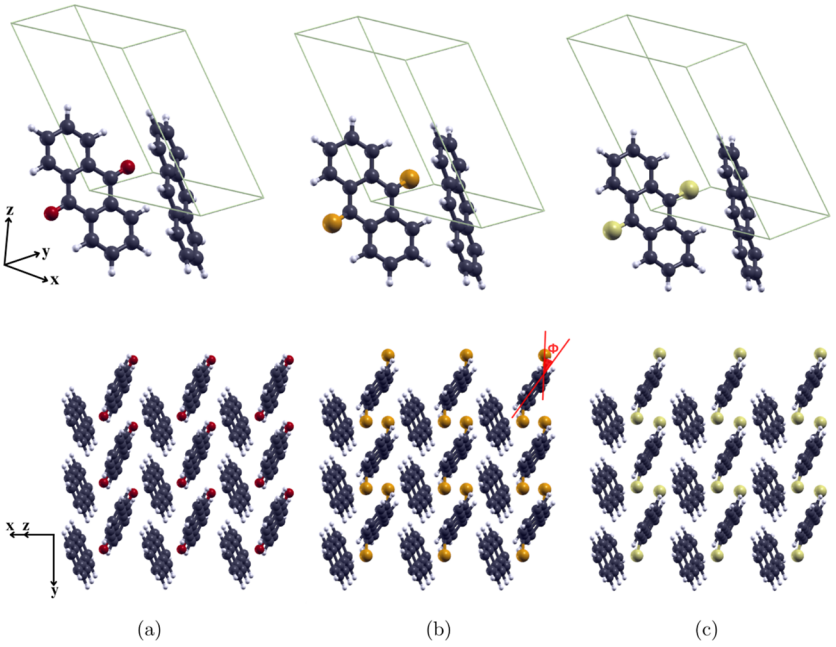

Figure 2. Primitive unit cell (first row) and 3 × 3 × 3 supercell (second row) of (a) O-doped anthracene, (b) P-doped anthracene, and (c) S-doped anthracene. The concept of the breakaway angle ϕ, which only applies to P-doped and S-doped anthracene, is illustrated in (b). Hydrogen atoms are depicted in white, carbon in gray, oxygen in red, phosphorus in orange, and sulfur in yellow.

Table 3. Lattice Constants (a, b, c), Unit Cell Volume (V), C−O Bond Length, and Herringbone Angle (θ) of O-Doped Anthracene under Various Applied Hydrostatic Pressures (Lattice Angles Were Kept Constant)

pressure (GPa)	a (bohr)	b (bohr)	c (bohr)	V (bohr^3)	C−O (bohr)	θ (deg)
5	15.383	10.820	20.094	2753.041	2.3204	130.702
8.75	14.929	10.501	19.501	2516.638	2.3196	131.656
10	14.818	10.423	19.356	2460.851	2.3194	131.859
15	14.475	10.181	18.908	2241.337	2.3185	132.591
20	14.225	10.006	18.581	2177.012	2.3188	132.986

respect to each other. Specifically, θ is defined as the angle formed by the two molecular planes.[28]

Table 2 presents the structural parameters for crystalline anthracene when different hydrostatic pressures up to 20 GPa were applied. Unit cell angles were kept constant during relaxation. Convergence tests yielded a kinetic energy cutoff of 21 hartree and a k-point mesh of 4 × 4 × 4. It is clear that as the applied pressure was increased, all three sides of the unit cell shrank. This agrees with an observed decrease in intermolecular distances as individual anthracene molecules moved closer to one another, resulting in stronger intermolecular forces. The decrease in C−H bond lengths also indicates a compression on the molecular level. However, even though hydrostatic pressure was increased at constant intervals of 5 GPa, the amount by which all lattice constants shrank became less as higher pressures were exerted. For instance, a decreased by 5.7% from the ambient case to the 5 GPa case, and subsequently by only 3.5% from 5 to 10 GPa. Even more noteworthy is the near-identical change in b and c. From ambient to 5 GPa of pressure, both b and c decreased by the same 5.7%; from 5 to 10 GPa, 3.5% again. This uniformity elucidates hydrostatic pressure's consistent impact on all three lengths of the unit cell, and also indicates the diminishing impact of larger pressures on lattice constants. Last, an increase in the herringbone angle demonstrates a readjustment in molecular orientations in response to shrinking unit cell lengths, and especially to the change in c since it was reduced the most from 21.112 Bohr to 18.441 Bohr.

Apart from pure anthracene, we studied three more systems: oxygen-doped anthracene, phosphorus-doped anthracene, and sulfur-doped anthracene. In selecting which elements to serve as dopants, we avoided metal elements and instead chose three earth-abundant nonmetals. This is in alignment with our current research's focus on organic materials.

https://doi.org/10.1021/acsomega.4c10572
ACS Omega 2025, 10, 4143−4153

Table 4. Lattice Constants (a, b, c), Unit Cell Volume (V), C−P Bond Length, Herringbone Angle (θ), and Breakaway Angle (ϕ) of P-Doped Anthracene under Various Applied Hydrostatic Pressures (Lattice Angles Were Kept Constant)

pressure (GPa)	a (bohr)	b (bohr)	c (bohr)	V (bohr^3)	C−P (bohr)	θ (deg)	ϕ (deg)
5	15.933	11.207	20.813	3059.232	3.3767	120.496	30.784
10	15.224	10.708	19.886	2668.599	3.3442	121.202	36.644
15	14.813	10.419	19.350	2458.321	3.3225	122.929	39.084
20	14.518	10.212	18.965	2314.555	3.3071	124.875	40.215

Table 5. Lattice Constants (a, b, c), Unit Cell Volume (V), C−S Bond Length, Herringbone Angle (θ), and Breakaway Angle (ϕ) of S-Doped Anthracene under Various Applied Hydrostatic Pressures (Lattice Angles Were Kept Constant)

pressure (GPa)	a (bohr)	b (bohr)	c (bohr)	V (bohr^3)	C−S (bohr)	θ (deg)	ϕ (deg)
2.5	16.651	11.712	21.751	3491.967	3.2841	128.141	16.915
5	15.925	11.201	20.802	3054.572	3.2622	126.099	22.956
10	15.213	10.701	19.872	2662.861	3.2348	127.227	28.205
15	14.814	10.420	19.351	2458.762	3.2171	128.030	30.870
20	14.526	10.217	18.975	2318.176	3.2059	128.781	32.812

Table 6. Band Gap Calculated Using DFT with GGA-PBE (E_g, in eV) and Corrected Band Gap Calculated Using Eq 1 (E_g^c, in eV) of the Four Studied Systems under Applied Hydrostatic Pressures up to 20 GPa, with Intervals of 5 GPa[a]

	pure		O-doped		P-doped		S-doped	
pressure (GPa)	E_g	E_g^c	E_g	E_g^c	E_g	E_g^c	E_g	E_g^c
5	1.802	2.581	1.048	1.559	1.012	1.510	0.692	1.077
10	1.649	2.374	0.852	1.293	0.689*	1.073*	0.471	0.777
15	1.531	2.214	0.696	1.082	0.450*	0.749*	0.318	0.570
20	1.415	2.056	0.583	0.929	0.270*	0.505*	0.204	0.415

[a]All band gaps are indirect except for those marked with an asterisk "*", which indicates a direct band gap.

For each dopant, we substituted the two hydrogen atoms located on the middle ring of one of the unit cell's two anthracene molecules, with the dopant atoms. This is illustrated in the first row of Figure 2. The kinetic energy cutoff for all three materials was taken to be 21 hartree and the k-point mesh was 4 × 4 × 4.

The relaxed structures of all doped materials retained the herringbone packing motif as well as the two-molecules-*per*-unit-cell arrangement. As presented in Tables 3, 4, and 5, all lattice constants and unit cell volumes of the doped materials experienced a decrease with rising hydrostatic pressure. This is further consolidated by the gradual reduction in intermolecular distance. Aside from compression on the crystal lattice, the compression of the molecules themselves is indicated by the reduction in the bond length between the dopant atom and carbon. The percentage decrease in all lattice constants of all three systems again displayed uniformity within the same interval of pressure, as well as a decreasing trend across different pressures. The major difference between these materials, then, lay in the conjugation of the doped molecules.

For O-doped anthracene, both molecules within the unit cell remained planar, possibly due to the similar atomic radii between hydrogen and oxygen, so that the substitution of the former by the latter had little effect on the molecular structure.

For P-doped anthracene, a significant break in the planar conjugation of the doped molecule was observed. As illustrated in the crystal structure diagram of Figure 2b, the breakaway angle ϕ is defined to be the angle by which the dopant atom (in this case, phosphorus) deviates from the original plane of the molecule. The shift can perhaps be explained by the attraction between phosphorus atoms between neighboring unit cells. All phosphorus atoms showcased the same ϕ under the same level of hydrostatic pressure, although we noticed an increase in ϕ as the applied pressure was increased, which could possibly have resulted from a rising herringbone angle. Meanwhile, the pure anthracene molecule within the unit cell stayed planar.

For S-doped anthracene, a similar break in the planar conjugation of the doped molecule was also present. Like the phosphorus's case, ϕ increased with applied pressure, though by comparing the breakaway angles of P-doped and S-doped anthracene, we found that sulfur atoms deviate less from the molecule's original plane than phosphorus atoms do at the same levels of hydrostatic pressure. That is, for the same applied hydrostatic pressure, ϕ of the P-doped anthracene was always greater than ϕ of the S-doped anthracene. The pure anthracene molecule in the unit cell remained planar.

3.2. Electronic Properties. Electronic properties are a crucial determinant of a solar cell's efficiency. The band gap of a material, which can be obtained from the electronic band structure, is an especially important factor since it determines what wavelengths of light can be absorbed by the material. Light emitted from the sun comes in photons of different wavelengths, and each wavelength corresponds to a specific amount of energy. Only photons containing an energy that is greater than the material's band gap will be absorbed by the material, exciting electrons in the valence band to the conduction band and permitting energy flow. According to the Shockley−Queisser limit, >30% solar cell efficiencies can be achieved with a band gap value between 1.0 and 1.6 eV, peaking at ∼34% for both 1.34 and 1.12 eV.[27] As presented in Table 6 and Figure 3, the corrected band gaps of crystalline anthracene under pressures up to 20 GPa are all greater than 2 eV, making this material in its pure form unsuitable for photovoltaic applications. However, the evolution of the band structures with increasing pressure displayed a decreasing trend

https://doi.org/10.1021/acsomega.4c10572
ACS Omega 2025, 10, 4143−4153

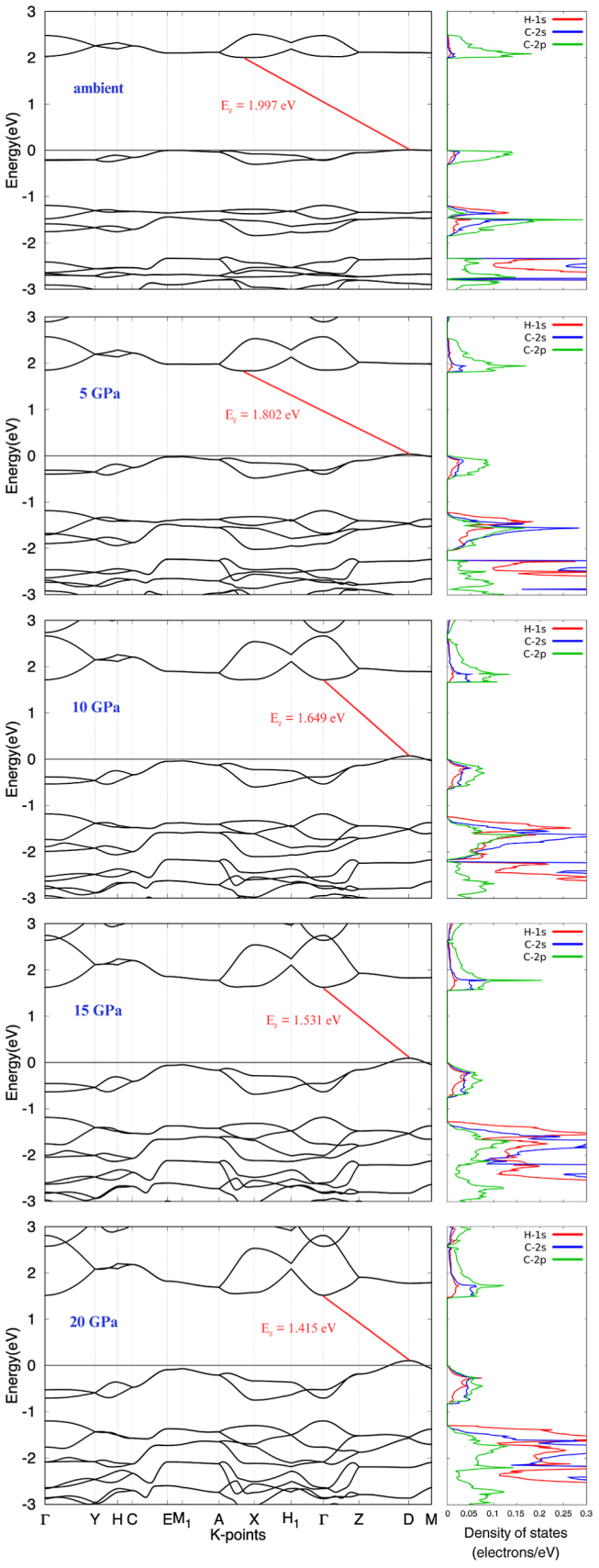

Figure 3. Band structure (left) and projected density of states (right) of pure anthracene under various applied hydrostatic pressures. The Fermi level is set to 0 eV for all plots.

in the band gap as the valence bands and the conduction bands shifted closer toward each other, in agreement with previous research.[28] The location of the conduction band minimum (CBM) remained unchanged at point D, although the valence band maximum (VBM) shifted from in between points A and X (at ambient pressure and 5 GPa) to Γ (at 10 GPa and greater pressures); nonetheless, this means that crystalline anthracene is an indirect band gap semiconductor. Meanwhile, a widening in the dispersion of bands is observed globally, indicating the increasing overlap in electron orbitals between neighboring atoms, which can be explained by how increasing pressure "pushes" the individual anthracene molecules closer toward each other within the crystal. These observations demonstrate the effectiveness of applying hydrostatic pressure at decreasing anthracene's band gap.

In addition to pressure, doping is another method of reducing the band gap. In our case, substituting two hydrogen atoms with two dopant atoms increases the number of free electrons within the material, which increases conductivity. Table 6 presents the DFT-calculated band gap and corrected band gap of the four studied systems under varying hydrostatic pressures up to 20 GPa, with intervals of 5 GPa. Additional pressure levels were calculated for the three doped systems so that they yielded close-to-optimal band gaps according to the Shockley−Queisser limit. The ambient case of pure anthracene was also calculated to serve as a benchmark to be later compared to. These additional data are displayed in Table 7.

Table 7. Pressure Level and Resulting Band Gaps (E_g and E_g^c) of the Four Materials for which Optical Properties will be Calculated[a]

system	pressure (GPa)	E_g (eV)	E_g^c (eV)
pure	ambient	1.997	2.845
O-doped	8.75	0.896	1.353
P-doped	10	0.689	1.073*
S-doped	2.5	0.887	1.341

[a]The pressure level that yielded a near-ideal band gap by the Shockley-Queisser limit[27] was chosen for each of the O-doped, P-doped, and S-doped anthracene systems; the ambient case of pure anthracene is also included to serve as a benchmark to be compared to later. All band gaps are indirect except for those marked with an asterisk "*", which indicates a direct band gap.

Figure 4 presents the band structures of O-doped crystalline anthracene under varying hydrostatic pressures. Corrected band gaps range from 0.929−1.559 eV, with 8.75 GPa yielding a near-ideal band gap of 1.353 eV. Comparing the band structures in Figure 4 to those in Figure 3, it is apparent that the doping of oxygen introduced additional bands to the original band gap region, hence significantly decreasing the band gap. Similar to pure anthracene's case, increasing pressures resulted in wider band dispersion and more overlap. The VBM and CBM remained at the high-symmetry *k*-points D and A, respectively, meaning O-doped anthracene is an indirect band gap semiconductor.

Band structures of P-doped anthracene under varying hydrostatic pressures are displayed in Figure 5. Corrected band gaps are within 0.505−1.510 eV, a large range compared to that of the other studied materials, indicating the greater tunability of P-doped anthracene. The material also shifts from having an indirect band gap at 5 GPa (VBM at C, CBM at E) to a direct band gap at 10 GPa and larger pressures (both VBM

https://doi.org/10.1021/acsomega.4c10572
ACS Omega 2025, 10, 4143−4153

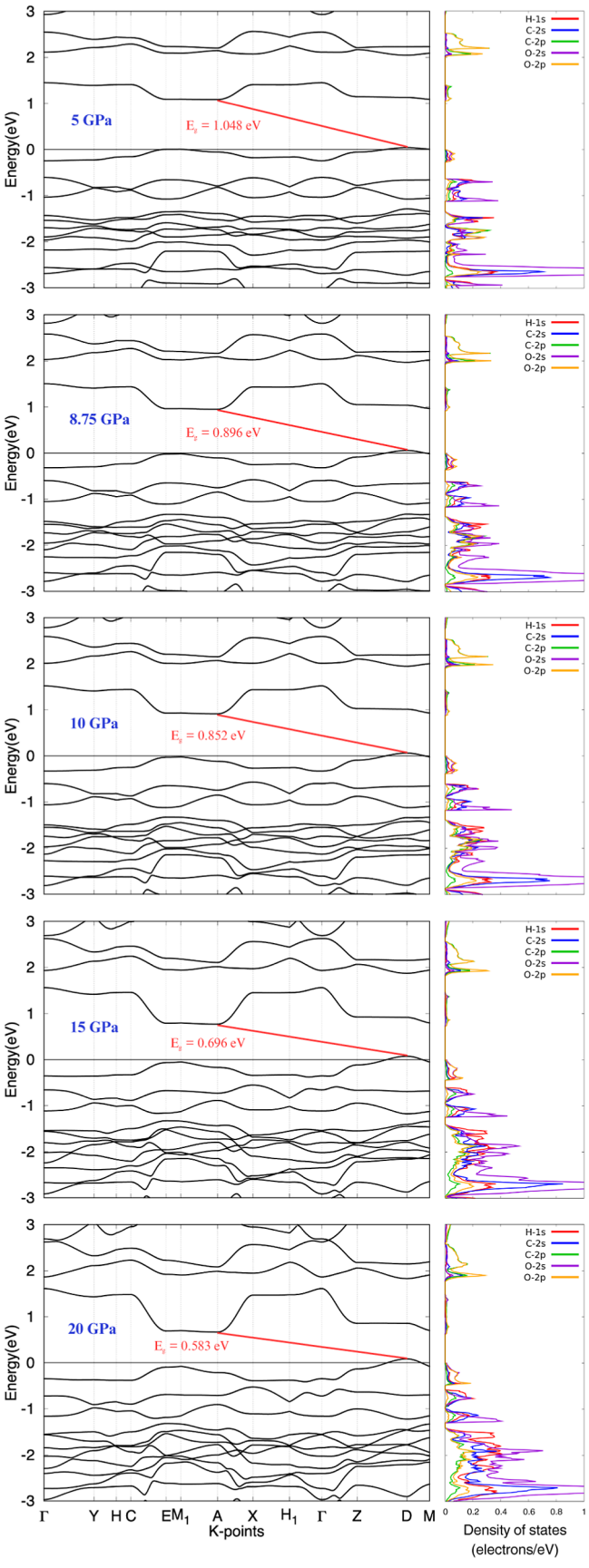

Figure 4. Band structure (left) and projected density of states (right) of O-doped anthracene under various applied hydrostatic pressures. The Fermi level is set to 0 eV for all plots.

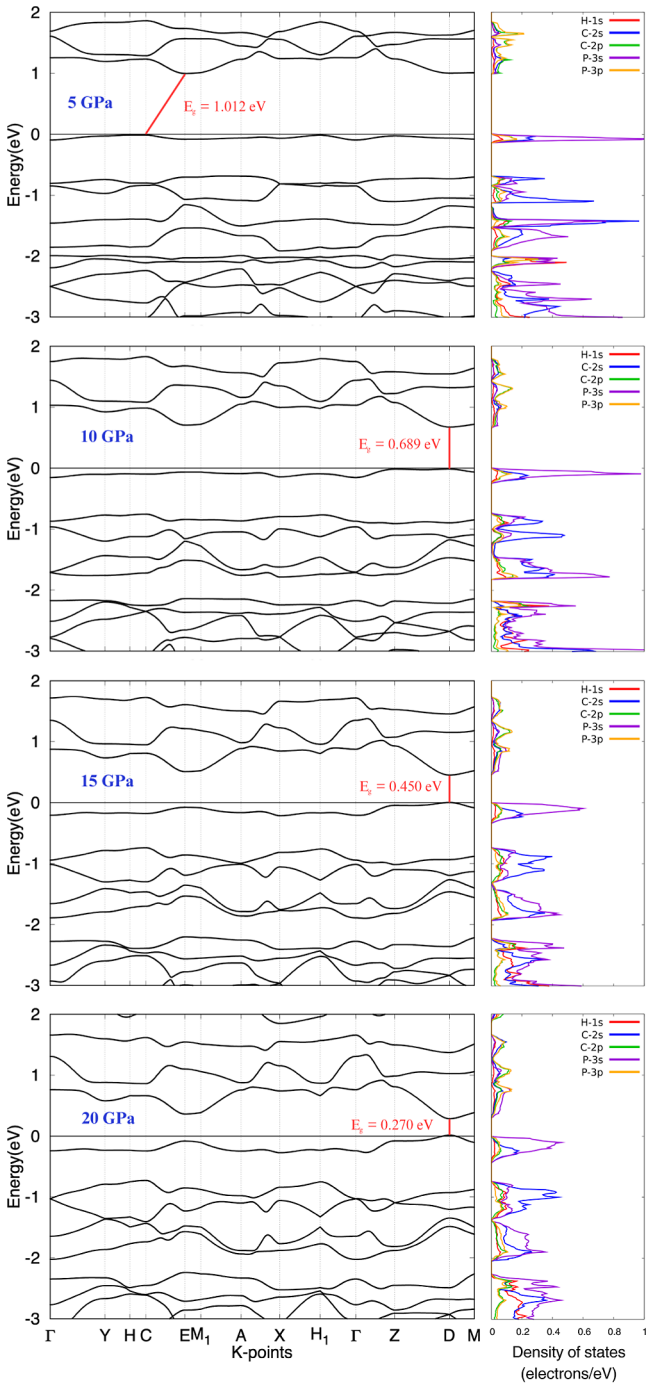

Figure 5. Band structure (left) and projected density of states (right) of P-doped anthracene under various applied hydrostatic pressures. The Fermi level is set to 0 eV for all plots.

and CBM occurring at point D). This is a significant change because direct band gaps eliminate the need for phonons during electronic transitions, enhancing the rate of photon absorption and solar cell efficiency.[44] A near-ideal band gap of 1.073 eV is found for P-doped anthracene under 10 GPa of pressure.

Figure 6 presents the band structures of S-doped anthracene under varying hydrostatic pressures. Corrected band gaps are in the range 0.415−1.341 eV, with 2.5 GPa yielding a near-ideal band gap of 1.341 eV. All band gaps are indirect (VBM at Γ and CBM at X). The evolution of band structures again

https://doi.org/10.1021/acsomega.4c10572
ACS Omega 2025, 10, 4143−4153

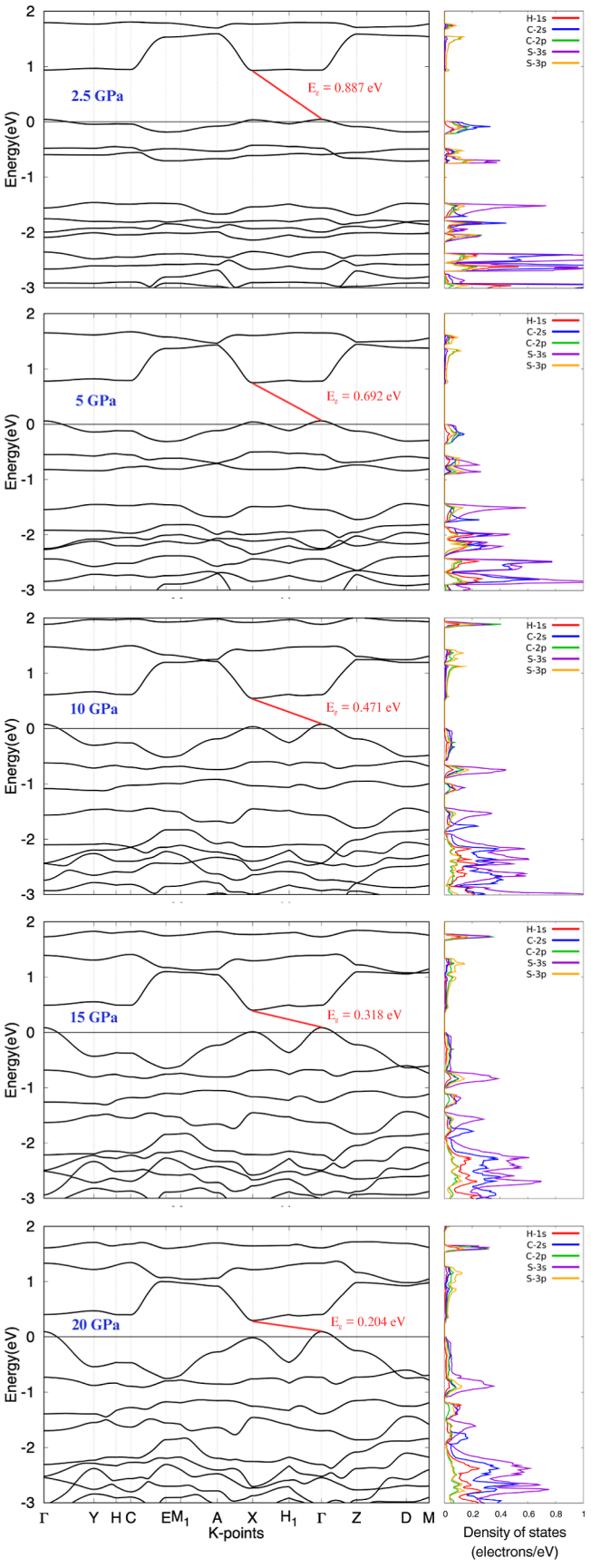

Figure 6. Band structure (left) and projected density of states (right) of S-doped anthracene under various applied hydrostatic pressures. The Fermi level is set to 0 eV for all plots.

demonstrates the effect of pressure on the nearing of valence and conduction bands toward each other. Band dispersion is increased as well.

To further understand the electronic band structure, we computed the projected density of states (PDOS) of all materials and presented them alongside the band structures in Figures 3−6. All PDOS plots demonstrate good agreement with their respective band structures in regards to correctly displaying the band gap and capturing bandwidths.

For pure anthracene, the H-1s and C-2s orbitals mainly account for the valence bands while the C-2p orbital contributes the most to the conduction bands. Specifically, at all pressure levels, both the VBM and CBM are dominated by the 2p orbitals of the carbon atom. The application of hydrostatic pressure prompts a significant increase in the density of the H-1s orbital within the valence bands.

In the case of O-doped anthracene, an increase in the density within conduction bands is observed, where the overlap between the curves of O-2p and C-2p orbitals implies nearly equal contributions to the conduction bands. The valence bands mostly result from the O-2s and C-2s orbitals. The VBM at all pressure levels is dominated by a roughly equal share of the 2s and 2p orbitals of the oxygen atom. Meanwhile, the CBM is nearly uniformly distributed among all atomic orbitals present.

For P-doped anthracene, P-3s and C-2s orbitals are mostly responsible for the valence bands, although increasing hydrostatic pressure diminishes their impact as demonstrated by the reduction in these two curves' peak densities. This points to a trend in which increasing pressure results in the broadening of bands, which is also accompanied by decreasing maxima of densities. The P-3p and C-2p orbitals account for most of the conduction bands. The VBM at all pressure levels is dominated by the 3s orbital of the phosphorus atom, while the CBM is dominated by the 3p orbital of the phosphorus atom.

In S-doped anthracene, the S-3s orbital contributes the most to valence bands while the conduction bands seem to result from a mixed combination of C-2p, S-3s, and S-3p orbitals. The application of increasing pressure again demonstrates the relationship between band broadening and reduced density peaks. For pressure levels up to 10 GPa, the VBM is dominated by the 2s orbital of the carbon atom. However, after 10 GPa, the VBM becomes dominated by the 3s orbital of the sulfur atom. The CBM is dominated by the 3p orbital of the sulfur atom throughout all pressure levels.

It is clear that a combination of doping and application of pressure significantly shrank down the rather large band gap of crystalline anthracene, resulting in modified materials that are suitable for photovoltaic applications. Having analyzed the electronic properties of the four systems under various applied pressures, we proceed to analyze the optical properties of the four selected materials displayed in Table 7.

3.3. Optical Properties. Optical properties are key indicators of the effectiveness of solar cell materials. In this section, we will analyze and discuss the dielectric function (ε) and the absorption coefficient (α).

The dielectric function describes a material's response to electromagnetic radiation. Specifically, the real part of the dielectric function describes the material's electronic polarizability while the imaginary part corresponds to light absorption.[45] Figure 7a,b present $\varepsilon_1(\omega)$ and $\varepsilon_2(\omega)$, respectively, for the four selected materials. The functions were

https://doi.org/10.1021/acsomega.4c10572
ACS Omega 2025, 10, 4143−4153

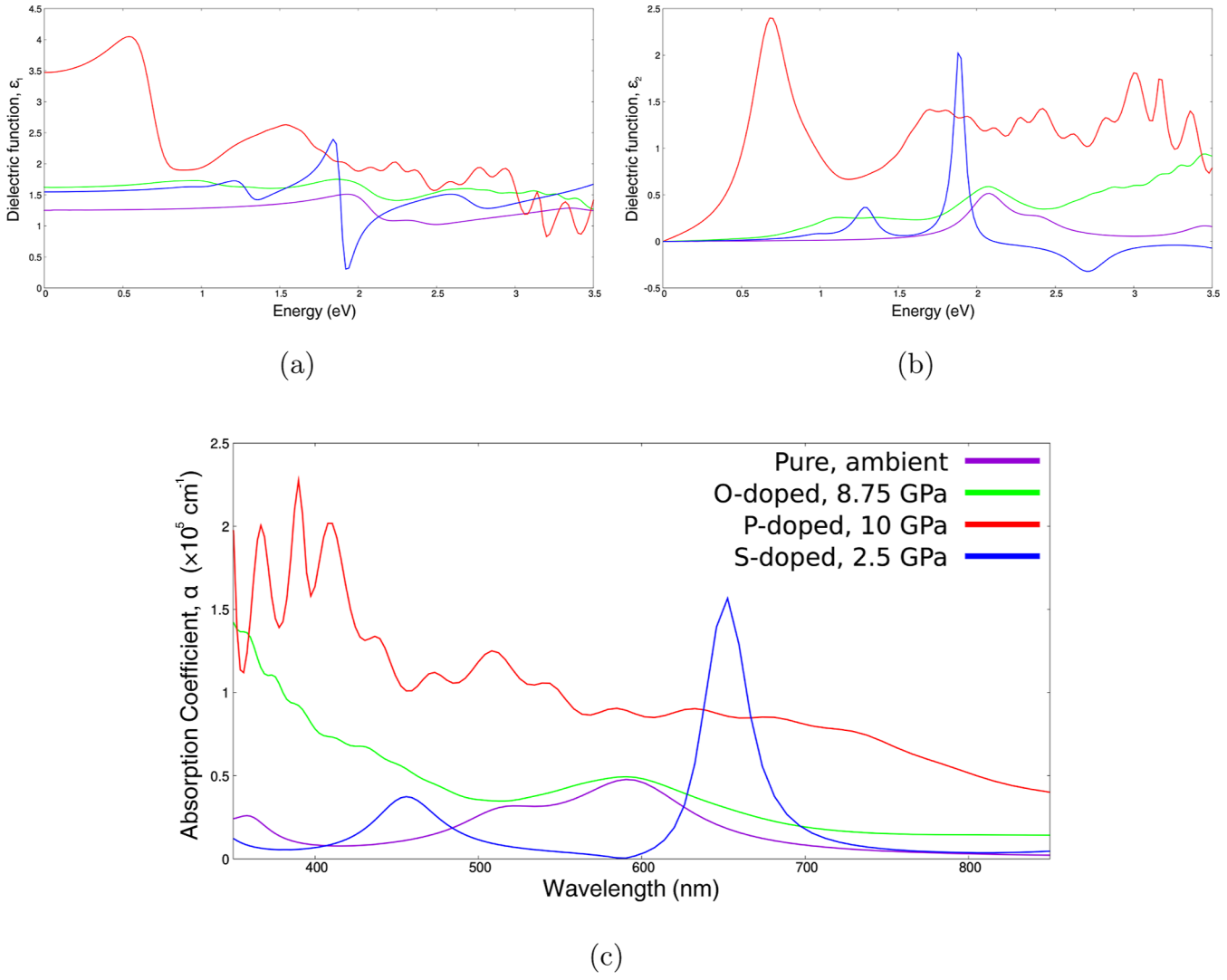

Figure 7. (a) The real part and (b) the imaginary part of the dielectric function of the four selected materials that were presented in Table 7. The pressure level of each of the three doped materials was chosen to yield a near-ideal band gap for photovoltaic application; the ambient anthracene was also included to serve as a benchmark to be compared to. Both graphs are plotted from the 0 to 3.5 eV range. (c) The absorption coefficient of the four selected materials, plotted from the 350 to 850 nm range (roughly corresponding to the visible light range).

plotted from 0 to 3.5 eV with intervals of 0.02 eV. The real parts of pure and O-doped anthracene demonstrate similar shapes, with the latter slightly shifted upward and both attaining minor peaks at around 1.90 eV. Additionally, both materials' imaginary parts start from zero and experience their first peaks at 2.07 eV, although after 2.50 eV the O-doped anthracene's curve increases while the pure anthracene's curve drops. The real curve of S-doped anthracene is quite close to that of pure anthracene from the 0 to 1.1 eV range, though it experiences a steep drop at around 1.90 eV. The first and second peaks of its imaginary curve occur at 1.28 and 1.88 eV, respectively. S-doped anthracene also displays negative values for $\varepsilon_2(\omega)$ after 2 eV, a phenomenon worth investigating in future studies. The real and imaginary parts of P-doped anthracene are significantly larger compared to the rest of the materials. Its real curve peaks first at 0.55 eV and then at 1.54 eV, showing a gradual decrease. Meanwhile, its imaginary curve peaks at 0.68 eV, with smaller peaks dispersed throughout higher energy ranges. There is a general trend in which materials with larger values for $\varepsilon_2(\omega)$ also exhibit a larger $\varepsilon_1(\omega)$. This can be attributed to the fact that a material interacts strongly with light at energy levels close to its band gap; this results in enhanced polarization and energy absorption near the band gap energy level, corresponding to a large $\varepsilon_1(\omega)$ and a large $\varepsilon_2(\omega)$, respectively.

The visible light range (380−700 nm) is usually the most important wavelength range to be considered for evaluating photovoltaic performance. This is because this range corresponds to maximum solar irradiance, meaning light of this wavelength range is most abundant on Earth and thus could contribute the most to generating solar energy.[46] Thus, we plotted the absorption coefficient α of the four selected materials on a similar range of 350−850 nm, as presented in Figure 7c. α dictates the depth in which light of a certain wavelength travels into a material before being absorbed, hence deciding the amount of energy that can be absorbed. It is clear that, compared to pure anthracene, the doped materials exhibit much higher absorption coefficients which are on the order of 10^5 cm^{-1} within certain energy ranges. These results are a whole order of magnitude greater than that of pure anthracene, proving the effectiveness of doping and using hydrostatic pressure as a means of modifying anthracene's optical

https://doi.org/10.1021/acsomega.4c10572
ACS Omega 2025, 10, 4143−4153

properties. S-doped anthracene shows rather low absorption coefficient values up until 600 nm, when it rises and peaks at 650 nm. O-doped anthracene peaks at the very beginning of the plot and decreases steadily until 510 nm, when it begins to rise to a minor peak at 590 nm that nearly touches the maximum of pure anthracene's curve, and drops off. The absorption coefficient of P-doped anthracene exhibits a global increase from the rest of materials, reaching above 10^5 cm^{-1} entirely from 350 to 530 nm. Three of its largest peaks occur at 367, 390, and 410 nm. The exceptional optical absorption ability of P-doped anthracene shows that a direct band gap can greatly improve absorption. O-doped and P-doped anthracene demonstrate what seems to be a redshift from pure anthracene since their absorption peaks all occur at shorter wavelengths. On the other hand, S-doped anthracene showcases a blueshift.

4. CONCLUSION

In this study, we used density functional theory (DFT) to investigate the effects of substitutional doping and hydrostatic pressure on the structural, electronic, and optical properties of crystalline anthracene. Various pressures up to 20 GPa were applied to four systems: pure anthracene, oxygen-doped anthracene, phosphorus-doped anthracene, and sulfur-doped anthracene. All lattice constants, unit cell volumes, and bond lengths displayed a decrease with pressure. All materials also exhibited a narrowing band gap with increasing pressure. While pure anthracene displayed band gaps greater than 2 eV, the doped materials exhibited significantly reduced band gaps between 0.415−1.559 eV, making many suitable for photovoltaic applications. In particular, three materials demonstrated optimal band gaps by the Shockley Queisser limit:[27] O-doped anthracene under 8.75 GPa (1.353 eV), P-doped anthracene under 10 GPa (1.073 eV), and S-doped anthracene under 2.5 GPa (1.341 eV). Calculations of their optical properties yielded enhanced values of the absorption coefficient on the order of 10^5 cm^{-1} within the visible light range, a significant improvement over pure anthracene.

Our research shows that the combination of substitutional doping and hydrostatic pressure is an effective means of tuning the electronic and optical properties of crystalline anthracene. We have successfully reduced its band gap and enhanced its absorption ability, making the modified materials ideal candidates for use in solar cells. Although the current research focuses on photovoltaics, we do not intend to exclude the possibility of anthracene's application beyond this field. Our research reveals the wide range of band gap values and absorption abilities that can be achieved by applying pressure to and doping anthracene, encouraging the material as well as other organic molecular crystals for use in other optoelectronic devices, such as the organic light-emitting diode (OLED) and the organic field-effect transistor (OFET). In addition, although it is likely that our results reflect real-world outcomes, future experimental work should be done to confirm our theoretical findings. With the many advantages of organic molecular crystals in mind, we hope that our work illuminates their great potential in photovoltaic applications as well as the path for future research in the improvement of organic photovoltaics and beyond.

■ ASSOCIATED CONTENT

Data Availability Statement

The data in this study are openly available in the Figshare repository at the following link: 10.6084/m9.figshare.28200380.v1.

■ AUTHOR INFORMATION

Corresponding Author

Congqing Yang − *National Graphene Research and Development Center, Springfield, Virginia 22151, United States;* orcid.org/0009-0007-5917-6130; Email: alexanderyang2026@gmail.com

Author

Xuan Luo − *National Graphene Research and Development Center, Springfield, Virginia 22151, United States;* orcid.org/0000-0002-0592-0610

Complete contact information is available at: https://pubs.acs.org/10.1021/acsomega.4c10572

Notes

The authors declare no competing financial interest.

■ ACKNOWLEDGMENTS

We would like to thank Dr. Gefei Qian for the technical support he provided throughout our research.

■ REFERENCES

(1) Rahman, A.; Murad, S. W.; Mohsin, A.; Wang, X. Does renewable energy proactively contribute to mitigating carbon emissions in major fossil fuels consuming countries? *J. Cleaner Prod.* **2024**, *452*, 142113.

(2) Perera, F.; Nadeau, K. Climate Change, Fossil-Fuel Pollution, and Children's Health. *N. Engl. J. Med.* **2022**, *386*, 2303−2314.

(3) Pastuszak, J.; Wegierek, P. Photovoltaic Cell Generations and Current Research Directions for Their Development. *Materials* **2022**, *15*, 5542.

(4) Andreani, L. C.; Bozzola, L. C.; Kowalczewski, P.; Liscidini, M.; Redorici, L. Silicon solar cells: toward the efficiency limits. *Adv. Phys.:X* **2019**, *4*, 1548305.

(5) Bhattacharya, S.; John, S. Beyond 30% Conversion Efficiency in Silicon Solar Cells: A Numerical Demonstration. *Sci. Rep.* **2019**, *9*, 12482.

(6) Alarifi, I. M. Advanced selection materials in solar cell efficiency and their properties - A comprehensive review. *Mater. Today: Proc.* **2023**, *81*, 403−414.

(7) Shah, N.; Shah, A. A.; Leung, P. K.; Khan, S.; Sun, K.; Zhu, X.; Liao, Q. A Review of Third Generation Solar Cells. *Processes* **2023**, *11*, 1852.

(8) Günes, S.; Neugebauer, H.; Sariciftci, N. S. Conjugated Polymer-Based Organic Solar Cells. *Chem. Rev.* **2007**, *107*, 1324−1338.

(9) Imahori, H.; Umeyama, T.; Ito, S. Large π-Aromatic Molecules as Potential Sensitizers for Highly Efficient Dye-Sensitized Solar Cells. *Acc. Chem. Res.* **2009**, *42*, 1809−1818.

(10) Kosco, J.; Moruzzi, F.; Willner, B.; McCulloch, I. Photocatalysts Based on Organic Semiconductors with Tunable Energy Levels for Solar Fuel Applications. *Adv. Energy Mater.* **2020**, *10*, 2001935.

(11) Hoppe, H.; Sariciftci, N. Organic solar cells: An overview. *J. Mater. Res.* **2004**, *19*, 1924−1945.

(12) Sun, P.; Liu, D.; Zhu, F.; Yan, D. An efficient solid-solution crystalline organic light-emitting diode with deep-blue emission. *Nat. Photonics* **2023**, *17*, 264−272.

(13) Kleemann, H.; Schuenemann, C.; Zakhidov, A. A.; Riede, M.; Lüssem, B.; Leo, K. Structural phase transition in pentacene caused by molecular doping and its effect on charge carrier mobility. *Org. Electron.* **2012**, *13*, 58−65.

(14) Lunt, R.; Benziger, J.; Forrest, S. Relationship between Crystalline Order and Exciton Diffusion Length in Molecular Organic Semiconductors. *Adv. Mater.* **2010**, *22*, 1233−1236.
(15) Wang, C.; Dong, H.; Jiang, L.; Hu, W. Organic semiconductor crystals. *Chem. Soc. Rev.* **2018**, *47*, 422−500.
(16) Park, S.; Kim, J.; Park, S. Organic 2D Optoelectronic Crystals: Charge Transport, Emerging Functions, and Their Design Perspective. *Adv. Mater.* **2018**, *30*, 1704759.
(17) Ohkita, H.; Tamai, Y.; Benten, H.; Ito, S. Transient Absorption Spectroscopy for Polymer Solar Cells. *IEEE J. Sel. Top. Quantum Electron.* **2016**, *22*, 100−111.
(18) Najafov, H.; Lee, B.; Zhou, Q.; Feldman, L.; Podzorov, V. Observation of long-range exciton diffusion in highly ordered organic semiconductors. *Nat. Mater.* **2010**, *9*, 938−943.
(19) Gélinas, S.; Rao, A.; Kumar, A.; Smith, S. L.; Chin, A. W.; Clark, J.; van der Poll, T. S.; Bazan, G. C.; Friend, R. H. Ultrafast Long-Range Charge Separation in Organic Semiconductor Photovoltaic Diodes. *Science* **2014**, *343*, 512−516.
(20) Sim, M.; Shin, J.; Shim, C.; Kim, M.; Jo, S. B.; Kim, J.; Cho, K. Dependence of Exciton Diffusion Length on Crystalline Order in Conjugated Polymers. *J. Phys. Chem. C* **2014**, *118*, 760−766.
(21) Verreet, B.; Heremans, P.; Stesmans, A.; Rand, B. Microcrystalline Organic Thin-Film Solar Cells. *Adv. Mater.* **2013**, *25*, 5504−5507.
(22) Watanabe, M.; Chen, K.; Chang, Y.; Chow, T. Acenes Generated from Precursors and Their Semiconducting Properties. *Acc. Chem. Res.* **2013**, *46*, 1606−1615.
(23) Chen, Y.; Wan, X.; Long, G. High Performance Photovoltaic Applications Using Solution-Processed Small Molecules. *Acc. Chem. Res.* **2013**, *46*, 2645−2655.
(24) Ambrosio, F.; Wiktor, J.; Landi, A.; Peluso, A. Charge Localization in Acene Crystals from Ab Initio Electronic Structure. *J. Phys. Chem. Lett.* **2023**, *14*, 3343−3351.
(25) Belkind, A. I.; Grechov, V. V. Energy levels of polyacene crystals. *Phys. Status Solidi A* **1974**, *26*, 377−384.
(26) Baessler, H.; Killesreiter, H. Bandgap-Determination from Autoionization Data in Molecular Crystals. *Mol. Cryst. Liq. Cryst.* **1973**, *24*, 21−31.
(27) Shockley, W.; Queisser, H. J. Detailed Balance Limit of Efficiency of p-n Junction Solar Cells. *J. Appl. Phys.* **1961**, *32*, 510−519.
(28) Fedorov, I. A. First-principles study of band structures of anthracene and tetracene under pressure. *Mater. Chem. Phys.* **2017**, *199*, 173−178.
(29) Hummer, K.; Puschnig, P.; Ambrosch-Draxl, C. Ab initio study of anthracene under high pressure. *Phys. Rev. B* **2003**, *67*, 184105.
(30) Muz, I.; Goktas, F.; Kurban, M. 3d-transition metals (Cu, Fe, Mn, Ni, V and Zn)-doped pentacene π-conjugated organic molecule for photovoltaic applications: DFT and TD-DFT calculations. *Theor. Chem. Acc.* **2020**, *139*, 23.
(31) Gonze, X.; et al. ABINIT: First-principles approach of materials and nanosystem properties. *Comput. Phys. Commun.* **2009**, *180*, 2582−2615.
(32) Blochl, P. Projector augmented-wave method. *Phys. Rev. B* **1994**, *50*, 17953−17979.
(33) Holzwarth, N. A. W.; Tackett, A. R.; Matthews, G. E. A Projector Augmented Wave (PAW) code for electronic structure calculations, Part I: atompaw for generating atom-centered functions. *Comput. Phys. Commun.* **2001**, *135*, 329−347.
(34) Groom, C. R.; Bruno, I. J.; Lightfoot, M. P.; Ward, S. C. The Cambridge Structural Database. *Acta Crystallogr., Sect. B* **2016**, *72*, 171−179.
(35) Broyden, C. G. The Convergence of a Class of Double-rank Minimization Algorithms 1. General Considerations. *IMA J. Appl. Math.* **1970**, *6*, 76−90.
(36) Fletcher, R. A new approach to variable metric algorithms. *Comput. J.* **1970**, *13*, 317−322.
(37) Goldfarb, D. A family of variable-metric methods derived by variational means. *Math. Comput.* **1970**, *24*, 23−26.
(38) Shanno, D. F. Conditioning of Quasi-Newton Methods for Function Minimization. *Math. Comput.* **1970**, *24*, 647−656.
(39) Morales-Garcia, A.; Valero, R.; Illas, F. An Empirical, yet Practical Way To Predict the Band Gap in Solids by Using Density Functional Band Structure Calculations. *J. Phys. Chem. C* **2017**, *121*, 18862−18866.
(40) Hua, H.; Luo, X. Pressure induced electronic and optical responses of vacancy-ordered double perovskites Cs2BX6 (B = Zr, Pd, Sn; X = Cl, Br, I). *Phys. Scr.* **2023**, *98*, 115520.
(41) Alam, S.; Saiduzzaman, M.; Biswas, A.; Ahmed, T.; Sultana, A.; Hossain, K. M. Tuning band gap and enhancing optical functions of AGeF3 (A = K, Rb) under pressure for improved optoelectronic applications. *Sci. Rep.* **2022**, *12*, 8663.
(42) Nishiwaki, M.; Fujiwara, H. Highly accurate prediction of material optical properties based on density functional theory. *Comput. Mater. Sci.* **2020**, *172*, 109315.
(43) Brock, C. P.; Dunitz, J. D. Temperature Dependence of Thermal Motion in Crystalline Anthracene. *Acta Crystallogr., Sect. B* **1990**, *46*, 795−806.
(44) Sreedevi, P.; Vidya, R.; Ravindran, P. Earth-abundant nontoxic direct band gap semiconductors for photovoltaic applications by ab-initio simulations. *Sol. Energy* **2019**, *190*, 350−360.
(45) Khan, W.; Betzler, S. B.; Šipr, O.; Ciston, J.; Blaha, P.; Scheu, C.; Minar, J. Theoretical and Experimental Study on the Optoelectronic Properties of Nb3O7(OH) and Nb2O5 Photoelectrodes. *J. Phys. Chem. C* **2016**, *120*, 23329−23338.
(46) Rottman, G. Measurement of Total and Spectral Solar Irradiance. *Space Sci. Rev.* **2007**, *125*, 39−51.

https://doi.org/10.1021/acsomega.4c10572
ACS Omega 2025, 10, 4143−4153